Resolving subcycle phase and amplitude modulation in strong-field ionization

Danish Furekh Dar,[1,*,†] Tao Chen,[2] Fang Liu,[2] and Stephan Fritzsche[1,3]

[1]*Helmholtz-Institut Jena, Fröbelstieg 3, D-07743 Jena, Germany*

[2]*Key Laboratory for Laser Plasmas (Ministry of Education) and School of Physics and Astronomy, Collaborative Innovation Center for IFSA, Shanghai Jiao Tong University, Shanghai 200240, China*

[3]*GSI Helmholtzzentrum für Schwerionenforschung GmbH, Planckstrasse 1, D-64291 Darmstadt, Germany*

(Received 28 May 2026; accepted 30 July 2026; published 12 August 2026)

Strong-field ionization in two-color ($\omega + 2\omega$) elliptically polarized laser fields highlights subcycle electron dynamics in the angular distribution of photoelectrons. In these distributions, a characteristic alternating angular pattern is observed, in which successive above-threshold ionization peaks and sidebands exhibit opposite angular shifts and are controllable through the relative phase between the two driving fields. This pattern originates from subcycle interference between adjacent ionization bursts, where a weak-field-induced phase modulation changes sign from one subcycle to the next, thereby directly controlling the emission angle. We further identify abrupt sideband shifts arising from the sensitivity to the relative phase between the two fields. Time-dependent Schrödinger equation simulations show that the long-range Coulomb interaction selectively suppresses electron emission counterrotating with respect to the driving field, with a pronounced dependence on the field helicity. These results establish angular shifts as a direct observable of subcycle phase modulation and demonstrate their utility as a sensitive interferometric probe of attosecond electron wave-packet dynamics.

DOI: 10.1103/61lb-rjd6

I. INTRODUCTION

Strong-field ionization underpins a broad range of ultrafast phenomena, including above-threshold ionization (ATI) [1–3], high-harmonic generation [4–7], laser-induced electron diffraction [8,9], nonsequential double ionization [10–12], and photoelectron holography [13–15], all of which are central to strong-field and attosecond physics. The emitted photoelectrons encode detailed information about both the ionization dynamics and the structural properties of atomic and molecular systems, making them powerful probes of ultrafast processes [16–19].

Bichromatic laser fields have emerged as versatile tools for controlling light-matter interactions [20–23], offering enhanced flexibility in steering processes such as terahertz emission [24,25] and the shaping of photoelectron wave packets [26,27]. In particular, two-color fields composed of a fundamental frequency and its second harmonic exhibit a tunable asymmetry that is governed by their relative phase. This phase-dependent waveform enables a wide range of applications, including molecular alignment [28] and coherent control of photoemission [29]. At the same time, the strong sensitivity of the field's temporal structure to the relative phase necessitates precise temporal characterization of the combined field.

More recently, circularly polarized two-color fields have opened new avenues for probing strong-field ionization dynamics [30]. These fields enable one to retrieve both the amplitude and phase of electron wave packets, as well as to access Wigner time delays [31–33]. In such configurations, the ionization dynamics are directly mapped onto the angular distributions of emitted photoelectrons, providing an efficient alternative to conventional pump-probe techniques that require time-delay scanning [34]. Moreover, circularly polarized fields combined with linearly polarized fields provide a powerful framework for resolving the subcycle ionization dynamics through angle-resolved photoelectron spectroscopy. In particular, the phase and amplitude of electron wave packets can be retrieved by analyzing the angular structure of photoelectron momentum distributions and thus enable the access to attosecond electron dynamics and tunneling-time information [35]. In such fields, angular structures in neighboring photoelectron peaks are identified as signatures of subcycle interference between adjacent ionization bursts [36]. Consequently, understanding the mechanisms governing these angular distributions has become a key objective.

Although two-color ω-2ω interferometry has been extensively explored in strong-field and attoclock physics, previous studies have just focused on retrieving ionization timing, wave-packet interference, or spatiotemporal shaping of photoelectron emission in circular or orthogonally polarized fields [31,34,35,37–41]. In contrast, the present work reveals a distinct alternating angular deflection of neighboring ATI and sideband (SB) peaks, originating from subcycle phase modulation between adjacent ionization bursts and controllable through the relative phase between the two driving fields.

*Present address: School of Physics and Astronomy, Shanghai Jiao Tong University, Shanghai 200240, China.

†Contact author: danishdar@sjtu.edu.cn

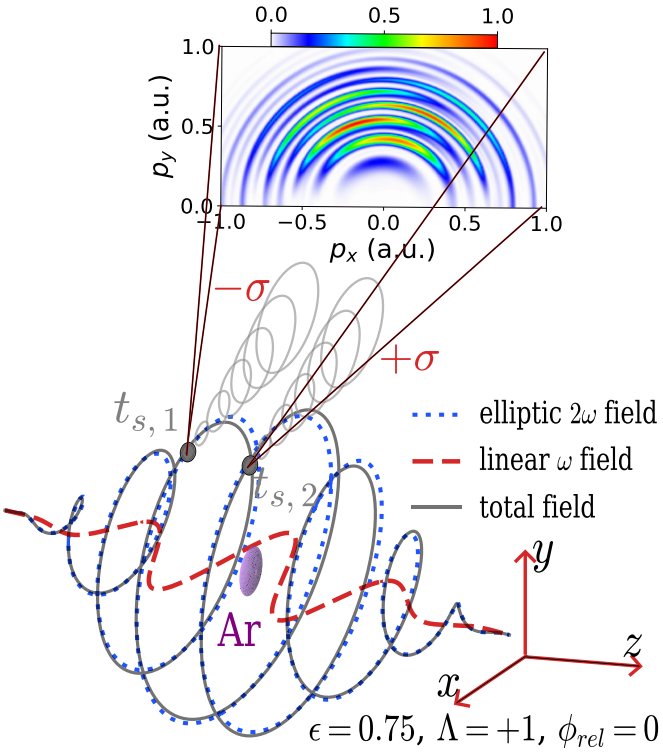

FIG. 1. Illustration of the two-color strong-field ionization mechanism considered in this work. The driving field consists of a strong elliptically polarized 2ω field of intensity 1.42×10^{14} W/cm^2, shown by the blue dotted curve, and a weak linearly polarized ω field of intensity 8.8×10^{11} W/cm^2, shown by the red dashed curve. Their coherent superposition gives the total electric field, indicated by the gray solid curve, which ionizes the Ar atom near adjacent subcycle field maxima. The two emitted electron wave packets, launched at the saddle times $t_{s,1}$ and $t_{s,2}$, acquire opposite weak-field-induced modulation phases, denoted by $-\sigma$ and $+\sigma$. The inset shows the resulting photoelectron momentum distribution in the polarization plane, where the subcycle phase modulation leads to angular deflections of the emitted electron signal. The field parameters are $\epsilon = 0.75$, $\Lambda = +1$, and $\phi_{\rm rel} = 0$.

We demonstrate that the weak-field-induced phase correction changes sign from one subcycle to the next and finally leads to complementary $\cos^2[\mathrm{Re}(\delta S)]$ and $\sin^2[\mathrm{Re}(\delta S)]$ interference conditions for ATI and sideband channels, respectively. The physical mechanism is summarized schematically in Fig. 1 where the weak fundamental field imprints opposite modulation phases on electron wave packets emitted at adjacent subcycle ionization times, leading to an angular modulation of the photoelectron signal. This establishes the observed angular shifts as direct signatures of subcycle phase modulation in bichromatic elliptically polarized fields. We further identify an abrupt sideband switching originating from the sensitivity to the relative phase between the two fields. Furthermore, with time-dependent Schrödinger equation (TDSE) simulations, we reveal how the long-range Coulomb interaction selectively suppresses counterrotating electron emission depending on the field helicity, thereby strongly modifying the interference structure. Our work therefore extends existing two-color interferometry as a probe of subcycle phase and amplitude modulation in strong-field ionization dynamics.

II. THEORETICAL FRAMEWORK

To explain the alternation of photoelctron spectra and the sideband switching, we consider a bichromatic laser field composed of a strong elliptically polarized second-harmonic field and a weak linearly polarized fundamental field. The total vector potential is written as $\mathbf{A}(t) = \mathbf{A}_{2\omega}(t) + \mathbf{A}_{\omega}(t)$, where $\mathbf{A}_{2\omega}(t) = -A_{2\omega}/\sqrt{1+\epsilon^2}\,[\cos(2\omega t)\hat{\mathbf{x}} + \epsilon\Lambda\sin(2\omega t)\hat{\mathbf{y}}]$ and $\mathbf{A}_{\omega}(t) = A_{\omega}\sin(\omega t + \phi_{\rm rel})\hat{\mathbf{x}}$. Here, $(A_{2\omega})$ and (A_{ω}) denote the field amplitudes, (ϵ) denotes the ellipticity, $(\Lambda = \pm 1)$ denotes the helicity of the (2ω) field, and $(\phi_{\rm rel})$ is the relative phase between the two colors.

Within the strong-field approximation (SFA) [42–44], the photoelectron amplitude is given by a coherent sum over saddle points [45], $M(\mathbf{p}) = \sum_s \Pi(t_s) e^{-iS(\mathbf{p},t_s)}$, where $\Pi(t_s)$ contains the ionization prefactor and the semiclassical action is $S(\mathbf{p}, t_s) = \int_{t_s}^{\infty}\{[\mathbf{p} + \mathbf{A}(t)]^2/2 + I_p\}dt$. The saddle points satisfy $[\mathbf{p} + \mathbf{A}(t_s)]^2/2 + I_p = 0$, with I_p the ionization potential.

Because the ω field is assumed to be much weaker than the elliptically polarized 2ω field, its contribution can be treated perturbatively by expanding the action as $S = S_0 + \delta S$, where S_0 is determined solely by $\mathbf{A}_{2\omega}(t)$. Keeping the leading corrections induced by A_{ω}, one obtains $\delta S = \int \Delta V(t)\,dt$, where $\Delta V(t) = \frac{A_{\omega}^2}{2}\sin^2(\omega t + \phi_{\rm rel}) + pA_{\omega}\cos\varphi_p\,\sin(\omega t + \phi_{\rm rel}) - \frac{A_{2\omega}A_{\omega}}{\sqrt{1+\epsilon^2}}\cos(2\omega t)\sin(\omega t + \phi_{\rm rel})$. Thus, $\Delta V(t)$ contains both terms linear in A_{ω} and a quadratic contribution proportional to A_{ω}^2. Using $\cos(2\omega t)\sin(\omega t + \phi_{\rm rel}) = \frac{1}{2}[\sin(3\omega t + \phi_{\rm rel}) - \sin(\omega t - \phi_{\rm rel})]$, the perturbation naturally separates into contributions oscillating at frequencies ω and 3ω.

The elliptically polarized 2ω field generates two ionization bursts per optical cycle, separated by a full cycle of the 2ω field, $t_2 = t_1 + \pi/\omega$. Consequently, neighboring trajectories experience opposite signs of the weak ω field. We therefore define the weak-field-induced phase accumulated between the two bursts as $2\delta S = -\int_{t_s}^{t_s+\pi/\omega}\Delta V(t)\,dt$, where t_s is the saddle point obtained in the absence of the weak field. Since the saddle time is complex, $t_s = t_r + it_i$, the correction δS also becomes complex and may be written as $\delta S = \mathrm{Re}(\delta S) + i\,\mathrm{Im}(\delta S)$. Physically, $\mathrm{Re}(\delta S)$ modifies the relative phase between neighboring ionization bursts, whereas $\mathrm{Im}(\delta S)$ changes their relative amplitudes and therefore governs the tunneling asymmetry.

We can interpret the ionization of an outgoing electron by the interference between two temporal slits. The two electron wave packets can be written as $\psi_1 = \psi_0 e^{i\delta S}$ and $\psi_2 = \psi_0 e^{-i(S^0_{2,1}+\delta S)}$, where $S^0_{2,1} = S_0(t_2) - S_0(t_1)$ denotes the unperturbed action difference between adjacent ionization bursts. For ATI, the unperturbed phase difference satisfies $S^0_{2,1} \simeq n\pi$, where n is the absorbed photon number. A detailed derivation of the complex modulation phase, including the explicit expressions for $\mathrm{Re}[\delta S]$ and $\mathrm{Im}[\delta S]$, is provided in Appendix A. Separating the complex phase into real and imaginary parts reveals two distinct modulation mechanisms. The amplitude contribution is given by $I_{\rm amp} = 4|\psi_0|^2\sinh^2[\mathrm{Im}(\delta S)]$, showing

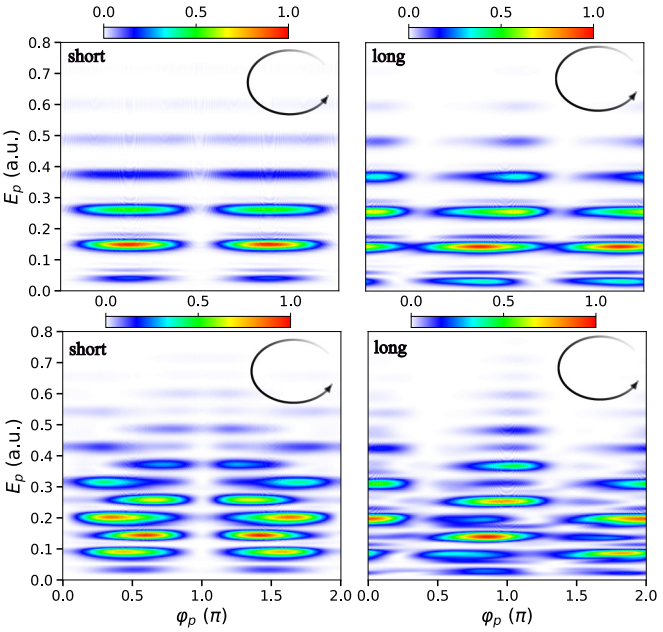

FIG. 2. Photoelectron momentum distributions in the polarization plane as functions of emission angle φ_p and energy E_p, obtained from numerical solutions of the TDSE. Top row: results for a single 2ω field, computed using short-range (left) and long-range (right) potentials. Bottom row: results for a two-color $\omega + 2\omega$ field with the same short-range (left) and long-range (right) potentials. The elliptically polarized 400-nm field (1.42×10^{14} W/cm^2) is combined with a weak linearly polarized 800-nm field (8.8×10^{11} W/cm^2) with relative phase $\phi_{\rm rel} = 0^\circ$. The black arrow indicate counterclockwise 2ω field rotation for $\Lambda = +1$. The color scale indicates the normalized yield.

that Im(δS) controls the relative strength of the two temporal slits and therefore governs the asymmetry of the electron emission. In contrast, the phase-dependent contribution becomes $I_{\rm ph} \propto 4|\psi_0|^2 \cos^2[{\rm Re}(\delta S)]$ for even n (ATI channels) and $I_{\rm ph} \propto 4|\psi_0|^2 \sin^2[{\rm Re}(\delta S)]$ for odd n (sideband channels). The complementary $\cos^2$ - $\sin^2$ structure therefore directly reflects the π phase shift between neighboring ionization bursts and explains the alternating angular modulation observed in the photoelectron momentum distributions.

III. RESULTS AND DISCUSSION

For the results presented below, we investigate strong-field ionization of Ar atoms within the single-active-electron approximation, using an ionization potential of $I_p = 15.76$ eV. The system is driven by an elliptically polarized 400-nm (2ω) laser field with ellipticity $\epsilon = 0.75$ and an intensity of 1.42×10^{14} W/cm^2. In the bichromatic configuration, the strong 2ω field is combined with a weak linearly polarized 800-nm (ω) field of intensity 8.8×10^{11} W/cm^2.

Figure 2 presents the photoelectron momentum distributions obtained from TDSE simulations for short-range and long-range binding potentials (Appendix B). The top row shows the spectra generated by the elliptically polarized 2ω field alone. For the short-range potential, the ATI peaks remain nearly symmetric with respect to the polarization axis,

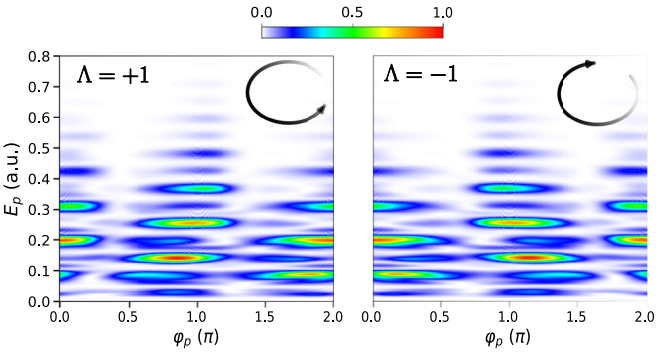

FIG. 3. Photoelectron momentum distributions in the polarization plane as a function of emission angle φ_p and energy E_p and for the helicity $\Lambda = +1$ (left) and -1 (right). The other parameters are the same as Fig. 2. The black arrow indicates counterclockwise and clockwise 2ω field rotation for $\Lambda = +1$ and -1, respectively. The color scale denotes the normalized yield.

reflecting the intrinsic symmetry of the laser-driven dynamics in the absence of long-range Coulomb effects. In contrast, the long-range potential introduces a clear angular shift of the ATI peaks in the direction of the field rotation. This shift originates from Coulomb-driven deflection of the outgoing electron trajectories during continuum propagation and becomes most pronounced for low-energy electrons.

The bottom row in Fig. 2 shows the corresponding spectra for the bichromatic $\omega + 2\omega$ field. For the short-range potential, the weak linearly polarized ω field breaks the half-cycle symmetry of the elliptically polarized 2ω field and generates clear alternating ATI and sideband structures. The ATI and sideband peaks are shifted in opposite angular directions, producing a characteristic staggered angular pattern across the spectrum. This behavior is consistent with the complementary interference terms $I_{\rm ATI} \propto \cos^2[{\rm Re}(\delta S)]$ and $I_{\rm SB} \propto \sin^2[{\rm Re}(\delta S)]$, which govern the phase-dependent modulation of the neighboring channels.

For the long-range potential, the Coulomb interaction substantially modifies the subcycle interference pattern. Besides inducing an overall angular deflection along the rotational direction of the elliptically polarized 2ω field, the Coulomb field strongly suppresses peaks emitted against the direction of rotation. Remarkably, this suppression can be reversed and controlled by changing the helicity of the driving field, as demonstrated in Fig. 3. This asymmetry arises from Coulomb-induced continuum dynamics, where counterrotating trajectories experience stronger Coulomb deceleration and reduced ionization probability, while corotating trajectories remain enhanced. Consequently, the interplay between subcycle interference and long-range Coulomb interaction produces a strongly asymmetric ATI-sideband structure in the TDSE spectra.

Figure 4 shows photoelectron momentum distributions in the polarization plane as a function of emission angle φ_p and energy E_p for two representative relative phases. The adjacent energy orders display opposite angular deflections and the deflection can be switched by changing the relative phase between the two fields.

This behavior is quantified in Fig. 5, where we extract the angular shift $\Delta\theta$ of individual peaks relative to the reference

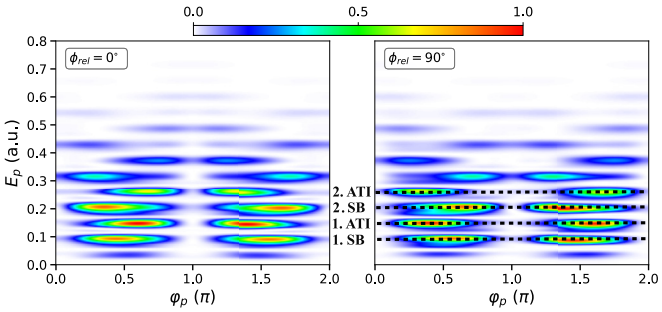

FIG. 4. Photoelectron momentum distributions in the polarization plane as a function of emission angle φ_p and energy E_p for relative phases $\phi_{\rm rel} = 0°$ (left) and 90° (right) calculated using SFA. The other parameters are the same as Fig. 2. The spectra display ATI peaks and SBs, indicated by dashed lines. The color scale denotes the normalized yield.

direction. The shifts oscillate with the relative phase $\phi_{\rm rel}$ and neighboring ATI and SB peaks exhibit opposite signs over the full phase range. This robust alternation indicates a parity-dependent interference mechanism.The amplitude and phase contributions are shown in Fig. 6. The amplitude term, governed by $\mathrm{Im}(\delta S)$, is symmetric in angle and does not produce any shift. In contrast, the phase contribution, controlled by $\mathrm{Re}(\delta S)$, exhibits pronounced angular asymmetry and determines the peak positions.

The parity dependence of the interference is directly reflected in the alternating structure of the phase term, which switches between $\cos^2(\mathrm{Re}\,\delta S)$ and $\sin^2(\mathrm{Re}\,\delta S)$ for even and odd orders, respectively. This leads to a reversal of angular asymmetry between neighboring peaks, consistent with the behavior observed in Fig. 4.

The persistence of this alternating behavior for different relative phases is demonstrated in Fig. 7. While the overall magnitude of the modulation varies with $\phi_{\rm rel}$, the sign reversal between adjacent ATI and SB peaks remains unchanged, confirming that it originates from the intrinsic symmetry of the interference.

Interestingly, the sidebands exhibit a pronounced sensitivity to the relative phase between the two fields. As shown in

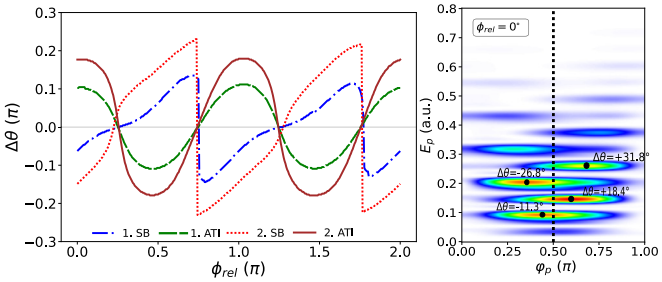

FIG. 5. Phase-dependent angular deflection of photoelectron peaks. Left: Angular shifts $\Delta\theta$ of the first and second ATI peaks and corresponding SB as a function of the relative phase $\phi_{\rm rel}$. Right: Photoelectron momentum distribution at $\phi_{\rm rel} = 0°$, illustrating the definition of the angular shift $\Delta\theta$ relative to the reference direction $\varphi_{\rm ref} = \pi/2$ (vertical dashed line). The marked points correspond to the peak positions used to extract $\Delta\theta$ for different ATI and SB orders. The other parameters are the same as in Fig. 2.

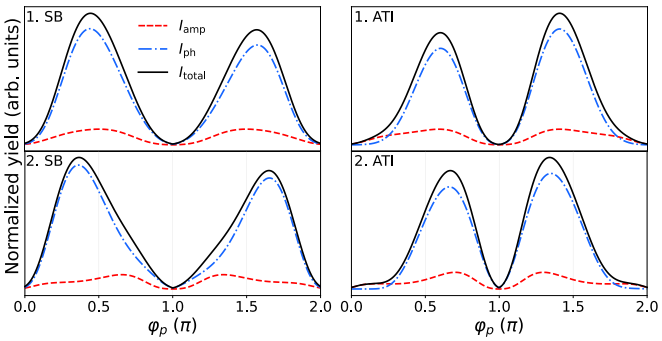

FIG. 6. The calculated yield of amplitude modulation $I_{\rm amp}$ (red dashed lines) and phase modulation $I_{\rm ph}$ (blue dash-dotted lines) for the first two sidebands (left column) and ATI peaks (right column) in the two-color field composed of an elliptically polarized 400-nm pulse and a weak linearly polarized 800-nm field. The black solid lines represent the total yield for each peak. We also consider $\phi_{\rm rel} = 0°$. The vertical axis shows the normalized yield and ranges from 0 to 1. Within each panel, the amplitude, phase, and total yields are normalized using the same maximum value of the total yield.

Fig. 7, their phase modulation develops a double-lobed structure that undergoes an abrupt switching as the relative phase is varied. In contrast, the ATI peaks display a predominantly single-lobed modulation that evolves smoothly with the relative phase. This qualitative difference directly accounts for the sudden angular displacements of the sidebands observed in Fig. 5.

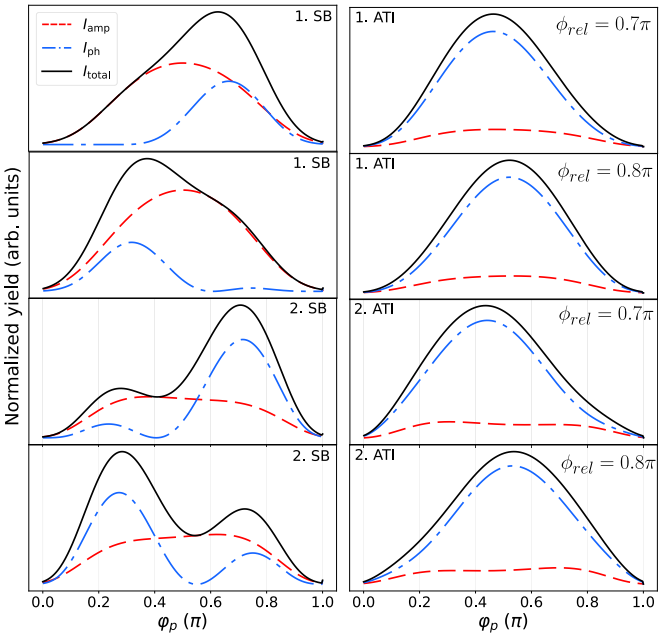

FIG. 7. The calculated yield of amplitude modulation $I_{\rm amp}$ (red dashed lines) and phase modulation $I_{\rm ph}$ (blue dash-dotted lines) for the first two sidebands and above-threshold-ionization peaks. The black solid lines represent the total yield for each peak. All other parameters are the same as Fig. 6 but for $\phi_{\rm rel} = 0.7\pi$ and 0.8π. The vertical axis shows the normalized yield and ranges from 0 to 1. Within each panel, the amplitude, phase, and total yields are normalized using the same maximum value of the total yield.

IV. CONCLUSIONS

We have shown that strong-field ionization in bichromatic elliptically polarized laser fields produces alternating deflections of neighboring photoelectron peaks. Successive ATI and sideband orders shift in opposite directions within the polarization plane, giving rise to a characteristic angular structure in the photoelectron momentum distribution. This behavior arises from the interference of the ionization amplitude as they arise from adjacent ionization bursts, where the weak-field-induced phase correction changes sign from one subcycle to the next. This results in parity-dependent interference conditions, manifested through alternating $\cos^2$ - $\sin^2$ modulation of the phase contribution. In contrast, the amplitude modulation remains symmetric and therefore does not contribute to the observed deflections. We further show that the sidebands exhibit a pronounced sensitivity to the relative phase between the two fields, leading to abrupt changes in their angular behavior. Time-dependent Schrödinger equation simulations additionally reveal that the long-range Coulomb interaction selectively suppresses electron emission counterrotating with respect to the driving field, with a clear dependence on the field helicity.

DATA AVAILABILITY

There are no publicly available research data or software supporting this manuscript. Requests for further information or data should be sent to the authors.

APPENDIX A: MODULATION PHASE FROM TWO-SLIT ELECTRON-WAVE-PACKET INTERFERENCE

In the two-slit picture, the measured sideband modulation originates from the interference of two electron wave packets emitted at two adjacent subcycle ionization times. For a field dominated by the 2ω component, these two ionization times are separated by half of the fundamental period:

$$t_{s,2} = t_{s,1} + \frac{T}{2}, \quad T = \frac{2\pi}{\omega}. \tag{A1}$$

Equivalently, this corresponds to one full optical cycle of the strong 2ω field.

The vector potentials are written as

$$\mathbf{A}_{2\omega}(t) = -\frac{A_{2\omega}}{\sqrt{1+\epsilon^2}}[\cos(2\omega t)\,\hat{\mathbf{x}} + \epsilon \sin(2\omega t)\,\hat{\mathbf{y}}], \tag{A2}$$

and

$$\mathbf{A}_{\omega}(t) = A_{\omega} \sin(\omega t + \phi_{\rm rel})\,\hat{\mathbf{x}}. \tag{A3}$$

The final momentum is

$$\mathbf{p} = p\cos\varphi_p\,\hat{\mathbf{x}} + p\sin\varphi_p\,\hat{\mathbf{y}}. \tag{A4}$$

The action accumulated between the two interfering emission times is

$$S_{2,1} = -\int_{t_{s,1}}^{t_{s,2}} \left[\frac{1}{2}[\mathbf{p} + \mathbf{A}_{2\omega}(t) + \mathbf{A}_{\omega}(t)]^2 + I_p\right] dt. \tag{A5}$$

Separating the action into the unperturbed 2ω contribution and the weak-field modulation gives

$$S_{2,1} = S_{2,1}^{(0)} + 2\delta S, \tag{A6}$$

where

$$S_{2,1}^{(0)} = -\int_{t_{s,1}}^{t_{s,2}} \left[\frac{1}{2}[\mathbf{p} + \mathbf{A}_{2\omega}(t)]^2 + I_p\right] dt, \tag{A7}$$

and the modulation phase is

$$2\delta S = -\int_{t_{s,1}}^{t_{s,2}} \left[[\mathbf{p} + \mathbf{A}_{2\omega}(t)] \cdot \mathbf{A}_{\omega}(t) + \frac{1}{2}\mathbf{A}_{\omega}^2(t)\right] dt. \tag{A8}$$

Substituting the explicit forms of the vector potentials gives

$$2\delta S = -\int_{t_{s,1}}^{t_{s,1}+T/2} \Bigg[pA_{\omega}\cos\varphi_p \sin(\omega t + \phi_{\rm rel}) - \frac{A_{2\omega}A_{\omega}}{\sqrt{1+\epsilon^2}} \cos(2\omega t)\sin(\omega t + \phi_{\rm rel}) \tag{A9}$$

$$+ \frac{1}{2}A_{\omega}^2 \sin^2(\omega t + \phi_{\rm rel})\Bigg] dt. \tag{A10}$$

Using

$$\cos(2\omega t)\sin(\omega t + \phi_{\rm rel}) = \tfrac{1}{2}[\sin(3\omega t + \phi_{\rm rel}) - \sin(\omega t - \phi_{\rm rel})], \tag{A11}$$

one obtains

$$\delta S = -\frac{\pi A_{\omega}^2}{8\omega} - \frac{pA_{\omega}\cos\varphi_p}{\omega}\cos(\omega t_{s,1} + \phi_{\rm rel}) + \frac{A_{2\omega}A_{\omega}}{2\sqrt{1+\epsilon^2}} \times \left[\frac{1}{3\omega}\cos(3\omega t_{s,1} + \phi_{\rm rel}) - \frac{1}{\omega}\cos(\omega t_{s,1} - \phi_{\rm rel})\right]. \tag{A12}$$

Now we write the complex saddle time as

$$t_s = t_r + i t_i. \tag{A13}$$

Using

$$\cos(x + iy) = \cos x \cosh y - i \sin x \sinh y, \tag{A14}$$

the real part of the modulation phase is

$$\mathrm{Re}[\delta S] = -\frac{\pi A_{\omega}^2}{8\omega} - \frac{pA_{\omega}\cos\varphi_p}{\omega}\cos(\omega t_r + \phi_{\rm rel})\cosh(\omega t_i) + \frac{A_{2\omega}A_{\omega}}{2\sqrt{1+\epsilon^2}}\left[\frac{1}{3\omega}\cos(3\omega t_r + \phi_{\rm rel})\cosh(3\omega t_i) - \frac{1}{\omega}\cos(\omega t_r - \phi_{\rm rel})\cosh(\omega t_i)\right]. \tag{A15}$$

The imaginary part is

$$\mathrm{Im}[\delta S] = \frac{pA_{\omega}\cos\varphi_p}{\omega}\sin(\omega t_r + \phi_{\rm rel})\sinh(\omega t_i) + \frac{A_{2\omega}A_{\omega}}{2\sqrt{1+\epsilon^2}}\left[-\frac{1}{3\omega}\sin(3\omega t_r + \phi_{\rm rel})\sinh(3\omega t_i) + \frac{1}{\omega}\sin(\omega t_r - \phi_{\rm rel})\sinh(\omega t_i)\right]. \tag{A16}$$

Thus, the weak ω field modifies the two adjacent electron wave packets as

$$\psi_1 = \psi_0 e^{i\delta S}, \quad \psi_2 = \psi_0 e^{-i\delta S - iS_{2,1}^{(0)}}. \tag{A17}$$

Consequently, Re[δS] controls the phase modulation, whereas Im[δS] controls the amplitude modulation of the two-slit electron-wave-packet interference.

APPENDIX B: TWO-DIMENSIONAL TDSE SIMULATIONS

To benchmark the SFA results and investigate the role of the binding potential, we solve the two-dimensional TDSE,

$$i\frac{\partial}{\partial t}\psi(\mathbf{r},t) = \left[-\frac{1}{2}\nabla^2 + V(\mathbf{r}) + \mathbf{r}\cdot\mathbf{E}(t)\right]\psi(\mathbf{r},t), \tag{B1}$$

where $\mathbf{r} = (x, y)$ and $\mathbf{E}(t)$ is the laser electric field.

Within the single-active-electron approximation, the atomic potential is modeled either by a long-range soft-core Coulomb potential,

$$V_{\mathrm{C}}(\mathbf{r}) = -\frac{1}{\sqrt{x^2+y^2+\eta}}, \tag{B2}$$

or by a short-range potential,

$$V_{\mathrm{SR}}(\mathbf{r}) = -\frac{1}{\sqrt{x^2+y^2+\eta}} e^{\left(-\frac{\sqrt{x^2+y^2}}{r_c}\right)}, \tag{B3}$$

where η is the soft-core parameter and r_c controls the range of the potential. For a fixed r_c, the soft-core parameter is varied to reproduce the ionization potential of Ar.

The initial ground state is obtained by imaginary-time propagation. The subsequent real-time propagation is performed using the split-operator method,

$$U(t+\Delta t, t) \approx e^{-i\frac{\Delta t}{2}V_{\mathrm{eff}}(t)} e^{-i\Delta t\frac{\hat{\mathbf{p}}^2}{2}} e^{-i\frac{\Delta t}{2}V_{\mathrm{eff}}(t)}, \tag{B4}$$

with

$$V_{\mathrm{eff}}(\mathbf{r},t) = V(\mathbf{r}) + xE_x(t) + yE_y(t). \tag{B5}$$

The kinetic propagation is evaluated in momentum space using fast Fourier transforms.

To extract the photoelectron momentum distribution, we employ a split-window (mask-function) technique,

$$F_s(r) = \frac{1}{1+\exp[-(r-R_s)/\Delta S]}, \tag{B6}$$

which separates the outgoing wave packet from the inner bound region. The outer wave packet is projected onto Volkov states,

$$C(\mathbf{p},t) = \frac{1}{2\pi}\int d^2r\, \psi_{\mathrm{out}}(\mathbf{r},t) e^{-i[\mathbf{p}+\mathbf{A}(t)]\cdot\mathbf{r}}, \tag{B7}$$

and accumulated during propagation as

$$M(\mathbf{p}, t+\Delta t) = e^{-i\Delta t\frac{1}{2}[\mathbf{p}+\mathbf{A}(t)]^2} M(\mathbf{p},t) + C(\mathbf{p},t). \tag{B8}$$

After the laser pulse, the photoelectron momentum distribution is obtained from

$$P(\mathbf{p}) = p\,|M(\mathbf{p})|^2. \tag{B9}$$

The simulations are performed on a 1024×1024 Cartesian grid covering 700×700 a.u.^{2}. The real-time propagation uses a time step $\Delta t = 0.02$ a.u., while the ground state is obtained by imaginary-time propagation with $\Delta\tau = 0.05$ a.u. The split-window radius is chosen as $R_s = 200$ a.u. with smoothing parameter $\Delta S = 8$ a.u.

[1] P. Agostini, F. Fabre, G. Mainfray, G. Petite, and N. K. Rahman, Free-free transitions following six-photon ionization of xenon atoms, Phys. Rev. Lett. **42**, 1127 (1979).

[2] J. Eberly, J. Javanainen, and K. K. Rzazęwski, Above-threshold ionization, Phys. Rep. **204**, 331 (1991).

[3] D. F. Dar, B. Minneker, and S. Fritzsche, Nondipole strong-field approximation for above-threshold ionization in a few-cycle pulse, Phys. Rev. A **107**, 053102 (2023).

[4] S. Ghimire and D. A. Reis, High-harmonic generation from solids, Nat. Phys. **15**, 10 (2019).

[5] G. Vampa, C. R. McDonald, G. Orlando, D. D. Klug, P. B. Corkum, and T. Brabec, Theoretical analysis of high-harmonic generation in solids, Phys. Rev. Lett. **113**, 073901 (2014).

[6] B. Minneker, B. Böning, A. Weber, and S. Fritzsche, Torus-knot angular momentum in twisted attosecond pulses from high-order harmonic generation, Phys. Rev. A **104**, 053116 (2021).

[7] J. Itatani, D. Zeidler, J. Levesque, M. Spanner, D. M. Villeneuve, and P. B. Corkum, Controlling high harmonic generation with molecular wave packets, Phys. Rev. Lett. **94**, 123902 (2005).

[8] C. I. Blaga, J. Xu, A. D. DiChiara, E. Sistrunk, K. Zhang, P. Agostini, T. A. Miller, L. F. DiMauro, and C. D. Lin, Imaging ultrafast molecular dynamics with laser-induced electron diffraction, Nature (London) **483**, 194 (2012).

[9] J. Xu, C. I. Blaga, A. D. DiChiara, E. Sistrunk, K. Zhang, Z. Chen, A.-T. Le, T. Morishita, C. D. Lin, P. Agostini, and L. F. DiMauro, Laser-induced electron diffraction for probing rare gas atoms, Phys. Rev. Lett. **109**, 233002 (2012).

[10] X. Liu and C. F. de M. Faria, Nonsequential double ionization with few-cycle laser pulses, Phys. Rev. Lett. **92**, 133006 (2004).

[11] J. B. Watson, A. Sanpera, D. G. Lappas, P. L. Knight, and K. Burnett, Nonsequential double ionization of helium, Phys. Rev. Lett. **78**, 1884 (1997).

[12] R. Kopold, W. Becker, H. Rottke, and W. Sandner, Routes to nonsequential double ionization, Phys. Rev. Lett. **85**, 3781 (2000).

[13] T. Khurelbaatar, J. Heo, S. Yu, X. Lai, X. Liu, and D. E. Kim, Strong-field photoelectron holography in the subcycle limit, Light Sci. Appl. **13**, 108 (2024).

[14] G. Porat, G. Alon, S. Rozen, O. Pedatzur, M. Krüger, D. Azoury, A. Natan, G. Orenstein, B. D. Bruner, M. J. J. Vrakking, and N. Dudovich, Attosecond time-resolved photoelectron holography, Nat. Commun. **9**, 2805 (2018).

[15] D. F. Dar and S. Fritzsche, Nonlinear interference and electron dynamics: Probing photoelectron momentum distributions in strong-field ionization, Phys. Rev. A **109**, L041101 (2024).

[16] M.-M. Liu, M. Li, C. Wu, Q. Gong, A. Staudte, and Y. Liu, Phase structure of strong-field tunneling wave packets from molecules, Phys. Rev. Lett. **116**, 163004 (2016).

[17] X.-B. Bian and A. D. Bandrauk, Attosecond time-resolved imaging of molecular structure by photoelectron holography, Phys. Rev. Lett. **108**, 263003 (2012).

[18] M. Han, P. Ge, Y. Shao, M.-M. Liu, Y. Deng, C. Wu, Q. Gong, and Y. Liu, Revealing the sub-barrier phase using a spatiotemporal interferometer with orthogonal two-color laser fields of comparable intensity, Phys. Rev. Lett. **119**, 073201 (2017).

[19] F. Lindner, M. G. Schätzel, H. Walther, A. Baltuška, E. Goulielmakis, F. Krausz, D. B. Milošević, D. Bauer, W. Becker, and G. G. Paulus, Attosecond double-slit experiment, Phys. Rev. Lett. **95**, 040401 (2005).

[20] S. Watanabe, K. Kondo, Y. Nabekawa, A. Sagisaka, and Y. Kobayashi, Two-color phase control in tunneling ionization and harmonic generation by a strong laser field and its third harmonic, Phys. Rev. Lett. **73**, 2692 (1994).

[21] J. L. Chaloupka and D. D. Hickstein, Dynamics of strong-field double ionization in two-color counterrotating fields, Phys. Rev. Lett. **116**, 143005 (2016).

[22] K. Lin, X. Jia, Z. Yu, F. He, J. Ma, H. Li, X. Gong, Q. Song, Q. Ji, W. Zhang, H. Li, P. Lu, H. Zeng, J. Chen, and J. Wu, Comparison study of strong-field ionization of molecules and atoms by bicircular two-color femtosecond laser pulses, Phys. Rev. Lett. **119**, 203202 (2017).

[23] C. A. Mancuso, K. M. Dorney, D. D. Hickstein, J. L. Chaloupka, J. L. Ellis, F. J. Dollar, R. Knut, P. Grychtol, D. Zusin, C. Gentry, M. Gopalakrishnan, H. C. Kapteyn, and M. M. Murnane, Controlling nonsequential double ionization in two-color circularly polarized femtosecond laser fields, Phys. Rev. Lett. **117**, 133201 (2016).

[24] L. Bergé, S. Skupin, C. Köhler, I. Babushkin, and J. Herrmann, 3D numerical simulations of THz generation by two-color laser filaments, Phys. Rev. Lett. **110**, 073901 (2013).

[25] K. Y. Kim, A. J. Taylor, J. H. Glownia, and G. Rodriguez, Coherent control of terahertz supercontinuum generation in ultrafast laser–gas interactions, Nat. Photon. **2**, 605 (2008).

[26] C. Ott, A. Kaldun, L. Argenti, P. Raith, K. Meyer, M. Laux, Y. Zhang, A. Blättermann, S. Hagstotz, T. Ding, R. Heck, J. Madroñero, F. Martín, and T. Pfeifer, Reconstruction and control of a time-dependent two-electron wave packet, Nature (London) **516**, 374 (2014).

[27] Y. Luo and P. Zhang, Ultrafast strong-field photoelectron emission due to two-color laser fields, Phys. Rev. B **98**, 165442 (2018).

[28] S. De, I. Znakovskaya, D. Ray, F. Anis, N. G. Johnson, I. A. Bocharova, M. Magrakvelidze, B. D. Esry, C. L. Cocke, I. V. Litvinyuk, and M. F. Kling, Field-free orientation of CO molecules by femtosecond two-color laser fields, Phys. Rev. Lett. **103**, 153002 (2009).

[29] M. Förster, T. Paschen, M. Krüger, C. Lemell, G. Wachter, F. Libisch, T. Madlener, J. Burgdörfer, and P. Hommelhoff, Two-color coherent control of femtosecond above-threshold photoemission from a tungsten nanotip, Phys. Rev. Lett. **117**, 217601 (2016).

[30] C. A. Mancuso, D. D. Hickstein, P. Grychtol, R. Knut, O. Kfir, X.-M. Tong, F. Dollar, D. Zusin, M. Gopalakrishnan, C. Gentry, E. Turgut, J. L. Ellis, M.-C. Chen, A. Fleischer, O. Cohen, H. C. Kapteyn, and M. M. Murnane, Strong-field ionization with two-color circularly polarized laser fields, Phys. Rev. A **91**, 031402(R) (2015).

[31] M. Han, P. Ge, Y. Shao, Q. Gong, and Y. Liu, Attoclock photoelectron interferometry with two-color corotating circular fields to probe the phase and the amplitude of emitting wave packets, Phys. Rev. Lett. **120**, 073202 (2018).

[32] D. Trabert, S. Brennecke, K. Fehre, N. Anders, A. Geyer, S. Grundmann, M. S. Schöffler, L. P. H. Schmidt, T. Jahnke, R. Dörner, M. Kunitski, and S. Eckart, Angular dependence of the Wigner time delay upon tunnel ionization of H_2, Nat. Commun. **12**, 1697 (2021).

[33] Z. Zhou, Y. Chen, Y. Li, Y. Tian, P. Ge, Y. Zhou, and P. Lu, Influence of electron-wave-packet amplitude and phase modulations on photoelectron angular distributions in strong-field ionization, Phys. Rev. A **112**, 063105 (2025).

[34] M. Han, P. Ge, J. Wang, Z. Guo, Y. Fang, X. Ma, X. Yu, Y. Deng, H. J. Wörner, Q. Gong, and Y. Liu, Complete characterization of sub-Coulomb-barrier tunnelling with phase-of-phase attoclock, Nat. Photon. **15**, 765 (2021).

[35] P. Ge, Y. Dou, M. Han, Y. Fang, Y. Deng, C. Wu, Q. Gong, and Y. Liu, Spatiotemporal imaging and shaping of electron wave functions using novel attoclock interferometry, Nat. Commun. **15**, 497 (2024).

[36] O. Pedatzur, G. Orenstein, V. Serbinenko, H. Soifer, B. D. Bruner, A. J. Uzan, D. S. Brambila, A. G. Harvey, L. Torlina, F. Morales, O. Smirnova, and N. Dudovich, Attosecond tunnelling interferometry, Nat. Phys. **11**, 815 (2015).

[37] Y. Guo, S.-J. Yan, C.-C. Cheng, X.-Y. Hao, A. Liu, and J. Guo, Interference structures of an Ar atom by orthogonally polarized laser pulses, Phys. Rev. A **111**, 053111 (2025).

[38] J. Tan, Y. Min, H. Lian, C. Liu, X. Hao, and M. He, Subcycle dynamics of temporal double-slit interference in strong-field tunneling ionization of H_2^+, Phys. Rev. A **110**, 043111 (2024).

[39] S. Yu, X. Lai, S. Xu, Y. Wang, L. Hua, W. Quan, and X. Liu, Nonadiabatic effect on temporal double-slit interference structures in an orthogonal two-color laser field, Phys. Rev. A **105**, 013116 (2022).

[40] J. M. Ngoko Djiokap, A. V. Meremianin, and N. L. Manakov, Electron interference in atomic ionization by two crossing polarized ultrashort pulses, Phys. Rev. A **103**, 023103 (2021).

[41] X. Xie, T. Wang, S. Yu, X. Lai, S. Roither, D. Kartashov, A. Baltuška, X. Liu, A. Staudte, and M. Kitzler, Disentangling intracycle interferences in photoelectron momentum distributions using orthogonal two-color laser fields, Phys. Rev. Lett. **119**, 243201 (2017).

[42] L. V. Keldysh, Ionization in the field of a strong electromagnetic wave, Sov. Phys. JETP **20**, 1307 (1965), https://www.jetp.ras.ru/cgi-bin/e/index/e/20/5/p1307?a=list.

[43] F. H. M. Faisal, Multiple absorption of laser photons by atoms, J. Phys. B: At. Mol. Phys. **6**, L89 (1973).

[44] H. R. Reiss, Effect of an intense electromagnetic field on a weakly bound system, Phys. Rev. A **22**, 1786 (1980).

[45] D. B. Milošević, G. G. Paulus, D. Bauer, and W. Becker, Above-threshold ionization by few-cycle pulses, J. Phys. B: At. Mol. Opt. Phys. **39**, R203 (2006).